Progress In Electromagnetics Research M, Vol. 115, 151–162, 2023

An Optimal Sparse Reconstruction Algorithm in Synthetic Aperture Interferometric Radiometer (SAIR)

Zilong Zhao, Zhongjian Fu, Jinguo Wang*, Zhaozhao Gao,
Jie Gu, Shiwen Li, Bo Qi, and Fan Jiang

Abstract—Synthetic aperture interferometric radiometer (SAIR) requires lots of antennas, receivers, and correlators to accurately reconstruct the brightness temperature (BT) distribution of the scene. Aiming to reduce the complexity of the hardware requirements in SAIR system while maintaining the image quality, a new optimal sparse reconstruction method is developed in this paper. Different from the existing imaging methods, the proposed method constructs the optimal receiving array with a few elements by evaluating the mutual coherence and the array factor of the sensing matrix in SAIR system, so as to achieve high-quality reconstruction of the BT image. Numerical simulations and experiments demonstrate that the proposed method can reconstruct the BT image by solely using a few receivers with higher image fidelity than the competing methods.

1. INTRODUCTION

Synthetic aperture interferometric radiometer (SAIR) has received much attention in recent years because it offers an effective way to increase the spatial resolution by using an array composed of small aperture antennas to synthesize a large aperture. In order to accurately recover the brightness temperature (BT) distribution of the scene, SAIR usually requires a large number of different samples in spatial frequency domain (called visibility samples) simultaneously to obtain as much information of the scene as possible [1]. For example, the microwave interferometric radiometer with aperture synthesis (MIRAS) system developed by the European space agency (ESA) contains 69 antennas, 72 receivers, and 72 analog to digital converters (ADCs) to measure the data [2]; the GeoSTAR-III system developed by the NASA Jet Propulsion Laboratory (JPL) employs 144 antennas, 144 receivers, and 144 ADCs to obtain the data [3]. The high system complexity and huge amount of data limit the application of SAIR in various domains such as remote sensing, surveillance, and military.

Aiming to solve the problem of the SAIR system with high complexity, a lot of research has been performed. These developed methods can be classified into three categories. One is based on the passive coding technology, one based on the clock scanning technology, and one based on the compressed sensing (CS) sparse reconstruction technology. For example, Kpré et al. proposed a passive coding technique to reduce the hardware cost of the SAIR system and the computation load [4–7]. However, the passive coding technique requires an oversized microwave cavity with uncorrelated transfer functions which will increase the volume of the SAIR system and limit the application of the SAIR in practice. Zhang et al. proposed an clock scan microwave interferometric radiometer (CSMIR) to reduce the array complexity [8, 9]. By rotating the sub-arrays with a small number of antennas, a complete visibility samples can be obtained and used to recover the BT maps. However, the CSMIR requires rotation equipment and is suitable for observing slow changing targets [9]. Li et al. proposed a CS approach

---

Received 30 December 2022, Accepted 28 February 2023, Scheduled 10 March 2023

* Corresponding author: Jinguo Wang (wangjinguo09@126.com).
The authors are with the Science and Technology on Electronic Information Control Laboratory, The 29th Research Institute of China Electronics Technology Group Corporation, Chengdu, Sichuan, China.

for reconstructing the BT images with less visibility samples [10]. The feasibility of the CS method in the SAIR system is demonstrated by simulations and experiments [10, 11]. However, the CS sparse reconstruction method in [10, 11] randomly selects some receivers from all receivers to recover the image. So, the imaging performance of the CS method in [10, 11] is not optimal.

The main contribution of this paper is to develop a new optimal sparse reconstruction method to reduce the complexity of the SAIR system while maintaining the image quality. The proposed method can obtain the optimal receiving array with a few elements by evaluating the mutual coherence and the array factor of sensing matrix in SAIR system. Therefore, the proposed method can achieve better imaging performance than the existing imaging methods with the same number of receivers.

This paper is organized as follows. In Section 2, a brief review of the CS sparse reconstruction method in SAIR system is firstly given. Then the factors which affect the performance of the CS sparse reconstruction method are studied and analyzed. Based on the analysis, the theory of the optimal sparse reconstruction method is presented. In Section 3, numerical simulations and experiments are given to validate the accuracy of the analysis and the feasibility of the proposed method. Conclusions are drawn in Section 4.

2. THEORY

2.1. Principle of the CS Sparse Reconstruction Method in SAIR

A brief review of the existing CS sparse reconstruction method in SAIR is given here. The measurement model of the SAIR is presented in Fig. 1.

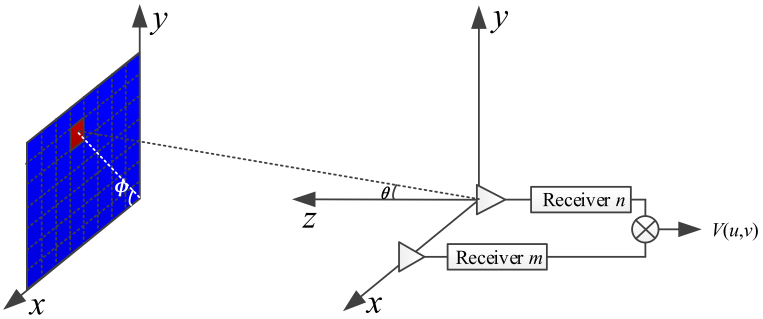

Figure 1. The measurement schematic of the SAIR.

Assume that the target source S is located at position (x_0, y_0, z_0), which is in the far field of the interferometer. The positions of receivers m and n are (x_m, y_m, z_m) and (x_n, y_n, z_n), respectively. The cross-correlation of the signals collected by these two receivers, namely visibility sample, is presented as follows according to the Van Cittert-Zernike theory [12–14]:

$$\begin{aligned} V(u,v,w) &= \iint_{\xi^2+\eta^2\le 1} \frac{\sqrt{D_m D_n} F_m(\xi,\eta) F_n^*(\xi,\eta)}{4\pi\sqrt{1-\xi^2-\eta^2}} T(\xi,\eta) \\ &\quad \cdot \exp\left[-j2\pi(u\cdot\xi + v\cdot\eta + w\cdot\sqrt{1-\xi^2-\eta^2})\right] d\xi d\eta \\ &= \iint_{\xi^2+\eta^2\le 1} T'(\xi,\eta)\cdot\exp\left[-j2\pi(u\cdot\xi + v\cdot\eta + w\cdot\sqrt{1-\xi^2-\eta^2})\right] d\xi d\eta \end{aligned} \quad (1)$$

where D_m and D_n are the antenna directivity, and $F_m(\xi,\eta)$ and $F_n(\xi,\eta)$ are the normalized antenna pattern of m and n, respectively. $(\xi,\eta) = (\sin\theta\cos\phi, \sin\theta\sin\phi)$, $u = (x_m - x_n)/\lambda$, $v = (y_m - y_n)/\lambda$, $w = (z_m - z_n)/\lambda$, $T(\xi,\eta)$ is the actual brightness temperature distribution, and $T'(\xi,\eta)$ is a modified brightness temperature distribution.

By discretization, Eq. (1) can be expressed as

$$V(u,v,w) = \sum_i \sum_j T'(\xi_i,\eta_j)\cdot\exp\left[-j2\pi(u\cdot\xi_i + v\cdot\eta_j + w\cdot\sqrt{1-\xi_i^2-\eta_j^2})\right], \quad (2)$$

When the receivers are located in the same x-y plane ($z_m = z_n$), Eq. (2) is simplified as follows:

$$V(u,v) = \sum_i \sum_j T'(\xi_i, \eta_j) \cdot \exp\left[-j2\pi(u \cdot \xi_i + v \cdot \eta_j)\right], \tag{3}$$

Rewrite Eq. (3) in the matrix form:

$$\mathbf{V}_{M\times 1} = \mathbf{G}_{M\times N}\mathbf{T'}_{N\times 1} \tag{4}$$

where

$$\mathbf{G}_{M\times N} = \begin{bmatrix} \exp([-j2\pi(u_1\xi_1 + v_1\eta_1)] & \cdots & \exp([-j2\pi(u_1\xi_N + v_1\eta_N)] \\ \exp[-j2\pi(u_2\xi_1 + v_2\eta_1)] & \cdots & \exp([-j2\pi(u_2\xi_N + v_2\eta_N)] \\ \vdots & \cdots & \vdots \\ \exp[-j2\pi(u_M\xi_1 + v_M\eta_1)] & \cdots & \exp([-j2\pi(u_M\xi_N + v_M\eta_N)] \end{bmatrix} \tag{5}$$

$\mathbf{G}_{M\times N}$ is the point spread function (PSF) of the system array, M the number of the system baseline ($M \leq I(I-1)/2$, I the number of receivers), and N the pixel number of the BT image.

According to the CS theory, the image $\mathbf{T'}$ can be recovered by solving the following convex optimization problem [10, 15–17]:

$$\min \|\mathbf{T'}\|_{l_1} \text{ s.t. } \|\mathbf{V} - \mathbf{\Phi}\mathbf{T'}\|_{l_2}^2 \leq \varepsilon \tag{6}$$

where the recovered image $\mathbf{T'}$ satisfies the sparsity requirement, and ε is the nonnegative real parameter. $\mathbf{\Phi}$ is the compressed measurement matrix and designed as follows [11]:

$$\mathbf{\Phi} = \mathbf{\Psi}\mathbf{G} = [\mathbf{\Psi}\mathbf{g}_1 \cdots \mathbf{\Psi}\mathbf{g}_n \cdots \mathbf{\Psi}\mathbf{g}_N] \tag{7}$$

where $\mathbf{g}_n$ is an $M \times 1$ column vector shown as follows:

$$\mathbf{g}_n = \begin{bmatrix} e^{-j2\pi(u_1\cdot\xi_n + v_1\cdot\eta_n)} \\ \vdots \\ e^{-j2\pi(u_m\cdot\xi_n + v_m\cdot\eta_n)} \\ \vdots \\ e^{-j2\pi(u_M\cdot\xi_n + v_M\cdot\eta_n)} \end{bmatrix} \quad (n = 1, \cdots, N) \tag{8}$$

$\mathbf{\Psi}$ is an $M \times 1$ column vector of random integers between 0 and 1, where the integer 1 in the mth row denotes the mth system baseline that is selected.

To the BT images which are not sparse, the transforms such as the discrete cosine transformation (DCT) and wavelet transformation are needed to firstly map the BT images to the sparse form [10]. Then the images in sparse form can be accurately reconstructed by using the state-of-the-art optimization methods [15, 18].

2.2. Optimal Sparse Reconstruction Method in SAIR

In light of the above theoretical descriptions, the performance of the CS sparse reconstruction method in SAIR mainly depends on the designed compressed measurement matrix $\mathbf{\Phi}$. According to the CS theory, the compressed measurement matrix $\mathbf{\Phi}$ should satisfy the restricted isometry property (RIP) condition [10, 16, 17] to guarantee the CS recovery capabilities. So, one key factor for designing the compressed measurement matrix $\mathbf{\Phi}$ is the mutual coherence of $\mathbf{\Phi}$ which is a computationally tractable measure for assessing whether the compressed measurement matrix $\mathbf{\Phi}$ satisfies the RIP condition [19]. In other words, the mutual coherence gives weaker guarantees of reconstruction than RIP, but is a more practical metric for assessing CS recovery properties [19]. In addition, another key factor for designing the compressed measurement matrix $\mathbf{\Phi}$ is the array factor (AF) of $\mathbf{\Phi}$ according to our research. This is because the AF represents the response of the receiving array [20]. The response of the receiving array, such as angular resolution and side lobe level of the antenna array, will affect the quality of the recovered image.

The mutual coherence μ and $\mathrm{AF}_{\mathrm{RMSE}}$ of the compressed measurement matrix $\mathbf{\Phi}$ are evaluated by following equations [10, 19, 20]:

$$\mu(\mathbf{\Phi}) = \max_{1\le i\ne j\le N} \frac{\left|\phi_i^H \phi_j\right|}{\|\phi_i\|_{l_2}\|\phi_j\|_{l_2}} \tag{9}$$

$$\mathrm{AF}_{\mathrm{RMSE}}(\mathbf{\Phi}) = \sqrt{\frac{1}{N}\sum_{n=1}^{N}\left|\sum_{m=1}^{M}\mathbf{g}_n(m) - \sum_{m=1}^{M}\mathbf{\Psi}(m)\mathbf{g}_n(m)\right|^2} \tag{10}$$

where ϕ_i is the ith column of $\mathbf{\Phi}$, M the total number of the system baseline, and N the total pixel number of the BT image. The lower the $\mu(\mathbf{\Phi})$ is, the stronger the incoherence of the compressed measurement matrix $\mathbf{\Phi}$ is, and the better the recover capability of CS is. The lower the $\mathrm{AF}_{\mathrm{RMSE}}(\mathbf{\Phi})$ is, the better the array response of $\mathbf{\Phi}$ is (or the lower the side lobe interference is).

To illustrate the correctness of the above analysis, Fig. 2 shows several different receiving array configurations. Fig. 2(a) shows a Y-shaped array which consists of 12 isotropic antennas with equal space of 20λ. Fig. 2(b)–Fig. 2(e) represent the layouts of receiving array formed by randomly selecting 8 elements from all 12 elements in Fig. 2(a), respectively. The mutual coherence and $\mathrm{AF}_{\mathrm{RMSE}}$ of these arrays in Fig. 2(b)–Fig. 2(e) are calculated according to Eq. (9) and Eq. (10).

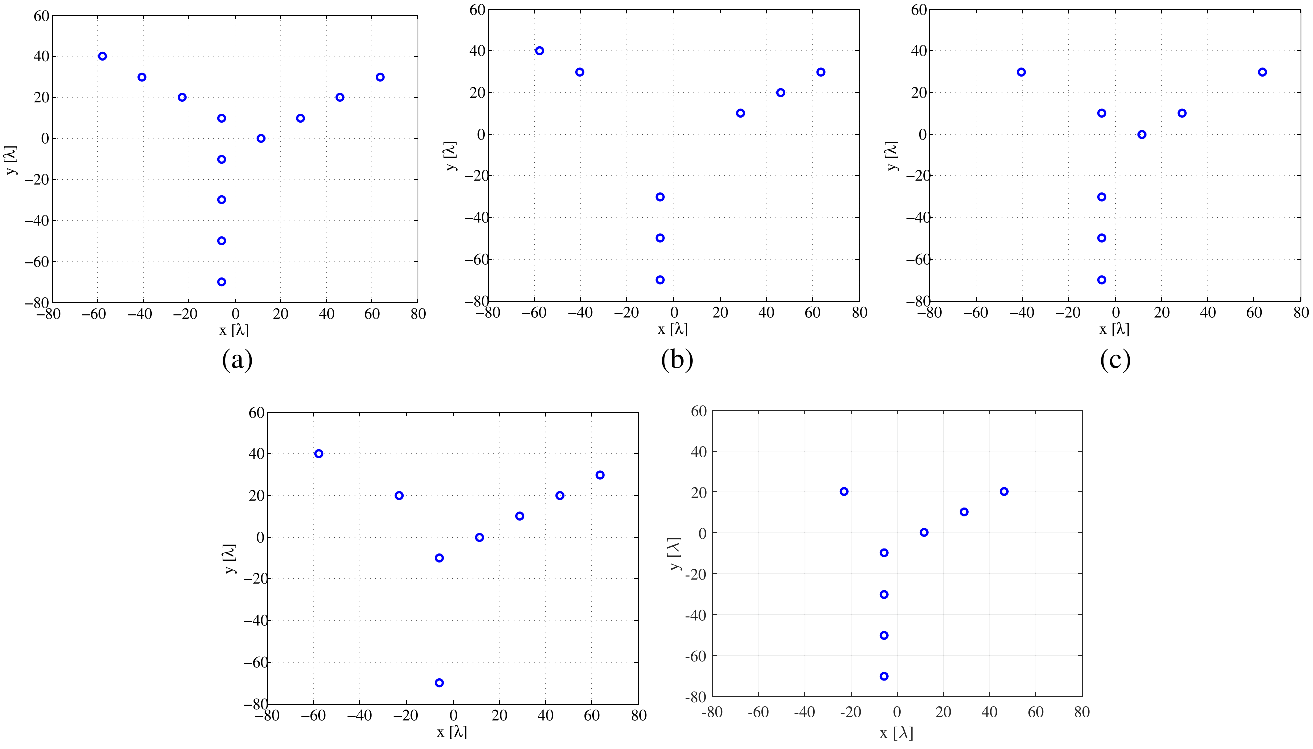

(a) (b) (c)

(d) (e)

Figure 2. (a) Original receiving array; (b) Receiving array with $\mu = 0.9897$ and $\mathrm{AF}_{\mathrm{RMSE}} = 0.10$; (c) Receiving array with $\mu = 0.9897$ and $\mathrm{AF}_{\mathrm{RMSE}} = 0.07$; (d) Receiving array with $\mu = 0.9897$ and $\mathrm{AF}_{\mathrm{RMSE}} = 0.13$; (e) Receiving array with $\mu = 0.9962$ and $\mathrm{AF}_{\mathrm{RMSE}} = 0.10$.

With the receiving array shown in Fig. 2(b)–Fig. 2(e), the results for recovering image of Fig. 3(a) are shown in Fig. 3(b)–Fig. 3(e), respectively. By comparing the results shown in Fig. 3(b)–Fig. 3(d), the image recovered by receiving array with lower $\mathrm{AF}_{\mathrm{RMSE}}$ has better quality when the mutual coherence of arrays is the same. This is because the receiving array with lower $\mathrm{AF}_{\mathrm{RMSE}}$ has a lower sidelobe, which can reduce the artifacts during the reconstruction. By comparing Fig. 3(b) and Fig. 3(e), the image

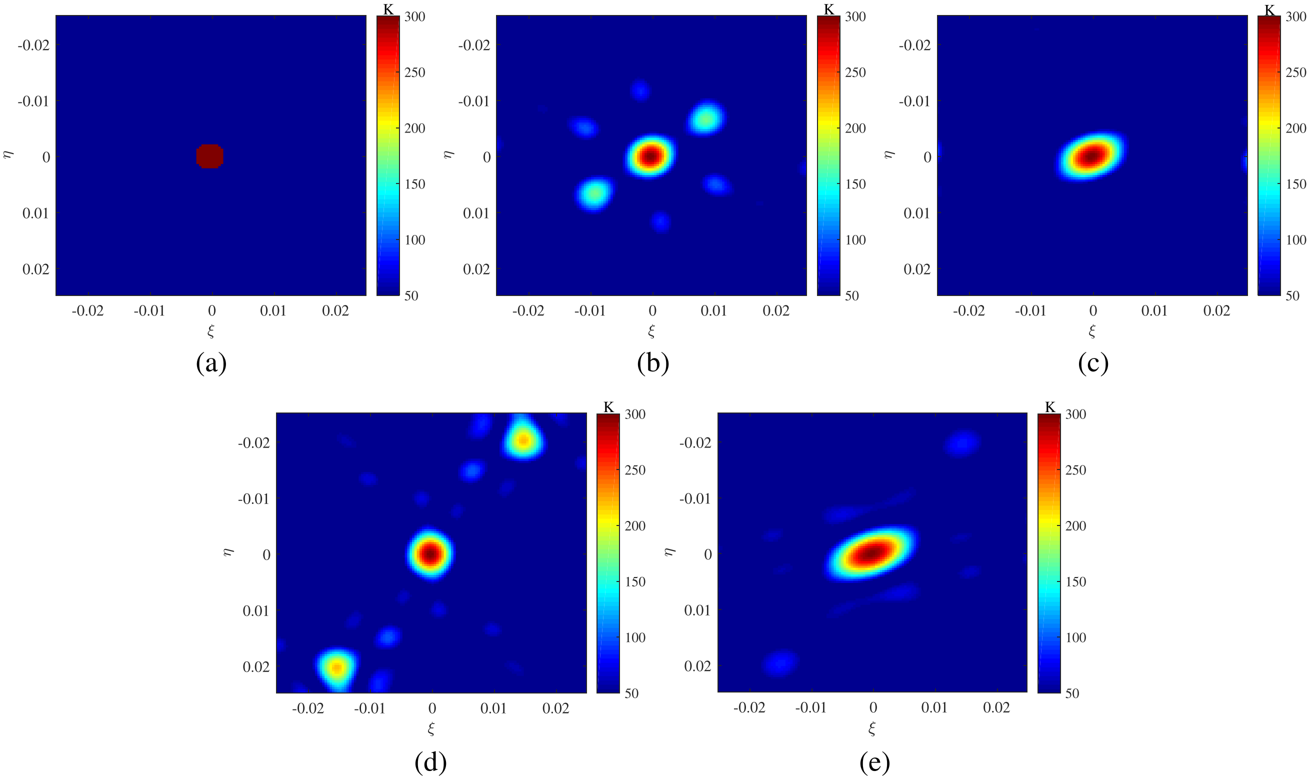

Figure 3. (a) Original BT image; (b) Image recovered with receiving array in Fig. 2(b); (c) Image recovered with receiving array in Fig. 2(c); (d) Image recovered with receiving array in Fig. 2(d); (e) Image recovered with receiving array in Fig. 2(e).

reconstructed by receiving array with lower value of mutual coherence has better quality when $\mathrm{AF}_{\mathrm{RMSE}}$ of these arrays are same.

Based on the above analysis, the criterion for designing the optimal compressed sensing matrix is presented as follows:

$$\mathbf{\Phi}_{\text{optimal}} = \min \left|\mathrm{AF}_{\mathrm{RMSE}}(\mathbf{\Phi}) \cdot \mu(\mathbf{\Phi})\right| \tag{11}$$

With the designed compressed measurement matrix $\mathbf{\Phi}_{\text{optimal}}$, the image can be recovered by using the gradient projection for sparse reconstruction (GPSR) algorithm [15] to solve the convex optimization equation shown in Eq. (6). The proposed method employs both the mutual coherence and the $\mathrm{AF}_{\mathrm{RMSE}}$ of the compressed measurement matrix as the design metric to obtain the optimal receiving array to recover the BT image with fewer receivers. The mutual coherence criterion (Eq. (9)) is used to ensure the effective solution of the sparse reconstruction, and the $\mathrm{AF}_{\mathrm{RMSE}}$ criterion (Eq. (10)) is used to ensure the optimal solution of the sparse reconstruction. In other words, the proposed method comprehensively considers the front-end array design and back-end processing to achieve the optimal reconstruction while the existing methods mainly consider the reconstruction from the perspective of back-end processing.

Figure 4 shows the flowchart of the proposed method. In Fig. 4, assume that the system receiving array consists of K antennas, and k antennas are selected to measure the data ($k \leq K$).

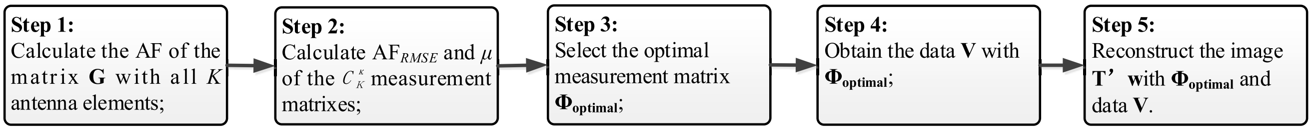

Figure 4. The flow chart of the proposed optimal sparse reconstruction method.

It is worth noting that the proposed method can still work even under the conditions of antenna elements with inconsistent radiation pattern, installation position error, etc. This is because the proposed method selects the optimal receiving elements to reconstruct by comparing the $\mathrm{AF}_{\mathrm{RMSE}}$ and mutual coherence of different array layouts. In practical application, the measured system array factor includes the influence of antenna radiation pattern, array element installation error, and other factors. Therefore, the method proposed in this paper has good applicability in practical engineering applications. Moreover, it is concluded that the performance of the nonlinear imaging algorithm is better than that of the linear imaging algorithm [16, 17]. So, the proposed method has better imaging performance than the traditional G-matrix method. This is because the traditional G-matrix method solves a linear problem while the proposed method solves a nonlinear problem as shown in Eq. (6).

3. SIMULATIONS AND EXPERIMENTS

3.1. Simulations for Imaging Earth and Ground Scenes

In this part, numerical scenarios for imaging earth and ground scenes with complex BT distribution are held to test the proposed method. Fig. 5(a) shows the original BT image of the earth with 173 × 173 pixels. Fig. 5(b) and Fig. 5(c) give the images reconstructed by using the methods in [19] and [11] with

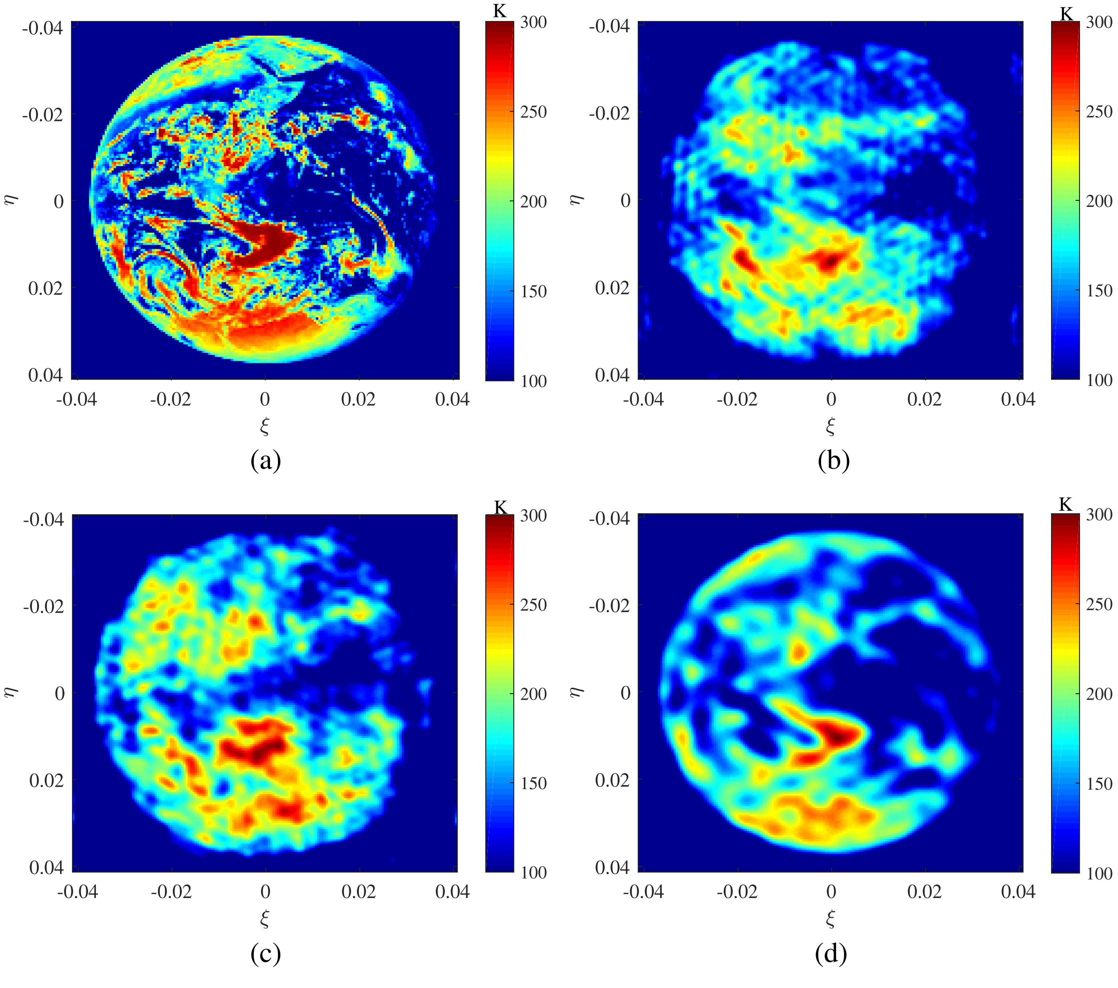

Figure 5. (a) Original BT image of the earth; (b) Image reconstructed by the method in [19] with 30 receivers; (c) Image reconstructed by the method in [11] with 30 receivers; (d) Image reconstructed by the proposed method with 30 receivers.

30 receivers, respectively. Fig. 5(d) shows the image reconstructed by using the proposed method with 30 receivers. By using the same number of receivers, the images reconstructed by the methods in [19] and [11] have much artifact while the image recovered by the proposed method agrees well with the original image.

In order to quantitatively evaluate the imaging performance of each method, the root mean square errors (RMSEs) of the results imaged by the three methods are calculated according to the following equation:

$$\mathrm{RMSE} = \sqrt{\frac{1}{N}\sum_{n=1}^{N}(\mathbf{T}(n) - \mathbf{T}'(n))^2} \tag{12}$$

where T is the original BT image of the scene, T' the BT image reconstructed by the imaging method, N the total pixel number of the BT image.

Table 1. RMSEs between the reconstructed images and the original image shown in Fig. 5.

	(b)	(c)	(d)
RMSE	0.3466	0.3532	0.3197

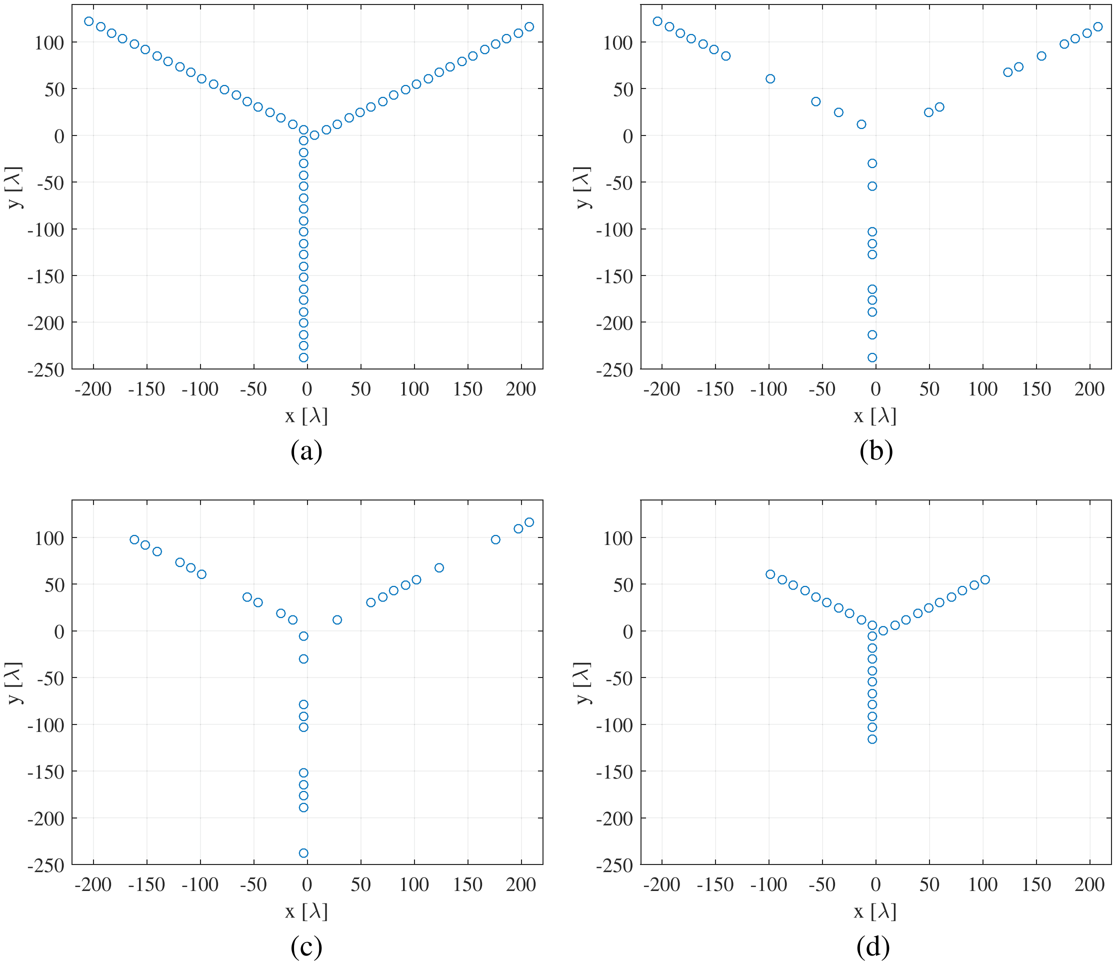

(a)

(b)

(c)

(d)

Figure 6. (a) Reference receiving array with 60 elements; (b) Receiving array designed by the method in [19] with 30 elements; (c) Receiving array designed by the method in [11] with 30 elements; (d) Receiving array designed by the proposed method in this paper with 30 elements.

Table 1 shows the RMSEs between the reconstructed images and the original image shown in Fig. 5. From Table 1, the image reconstructed by the proposed method has lower RMSE value than those reconstructed by the other methods.

Figure 6 shows the receiving array configurations used by the above three methods to reconstruct the images in Fig. 5. As reference, Fig. 6(a) shows the layout of a Y-shaped receiving array with 60 elements in SAIR system. Figs. 6(b)–6(c) present the receiving arrays designed by the existing methods in [19] and [11] with 30 elements, respectively. Fig. 6(d) shows the receiving array designed by the proposed method in this paper with 30 elements.

Figure 7(a) shows the ground scene with complex BT distribution. The size of Fig. 7(a) is 200×200 pixels. Fig. 7(b) gives the image reconstructed by using the method in [19] with the array shown in Fig. 6(b), and Fig. 7(c) gives the image reconstructed by using the method in [11] with the array shown in Fig. 6(c). Fig. 7(d) shows the image reconstructed by using the proposed method with the array shown in Fig. 6(d). From Fig. 7, the images reconstructed by the methods in [19] and [11] have much artifact while the image recovered by the proposed method agrees well with the original image.

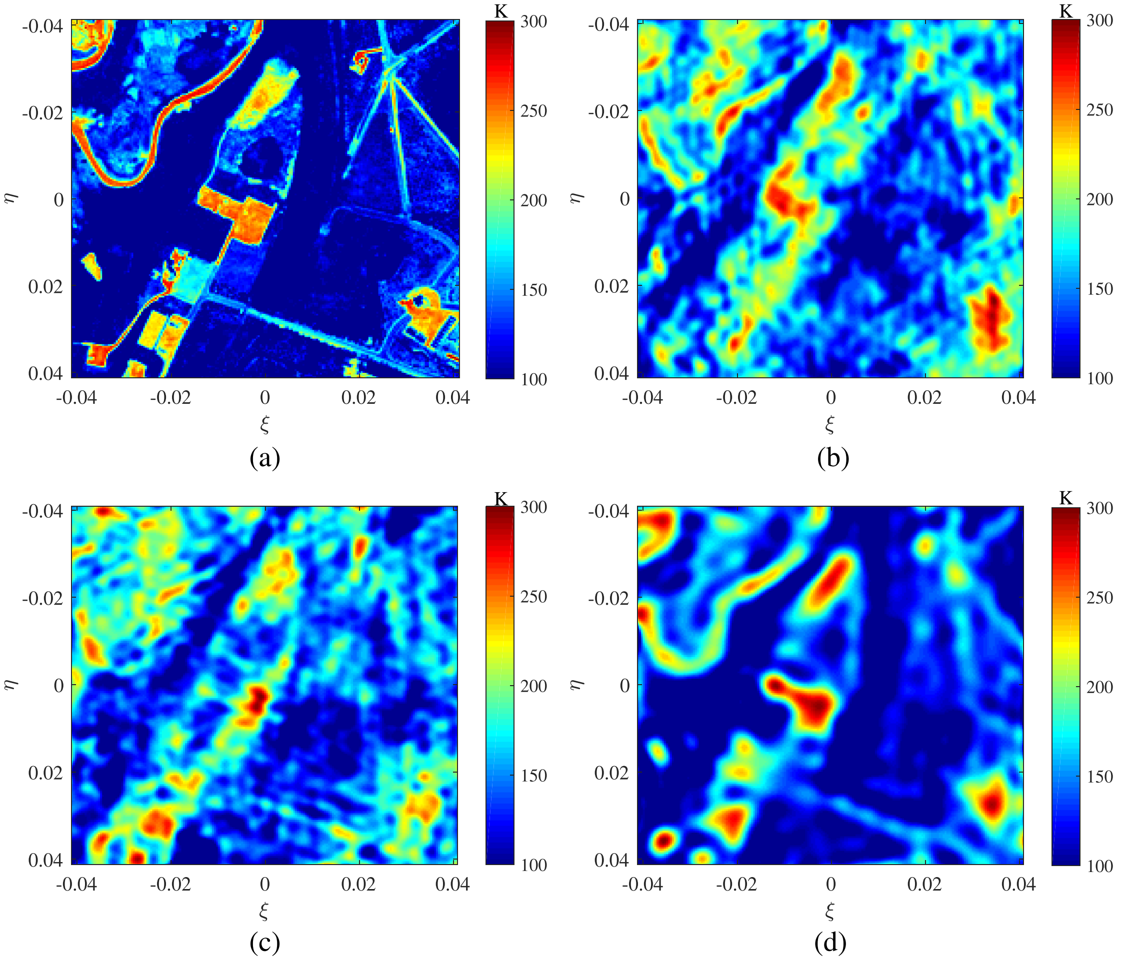

Figure 7. (a) Original BT image of the ground; (b) Image reconstructed by the method in [19] with 30 receivers; (c) Image reconstructed by the method in [11] with 30 receivers; (d) Image reconstructed by the proposed method with 30 receivers.

Table 2 lists the RMSEs between the reconstructed images and the original image shown in Fig. 7. From Table 2, the image reconstructed by the proposed method has lower RMSE value than those reconstructed by the other methods.

Compared with the existing methods, the proposed method can more accurately recover the image

Table 2. RMSEs between the reconstructed images and the original image shown in Fig. 7.

	(b)	(c)	(d)
RMSE	0.4602	0.5323	0.3789

with complex BT distribution. This is because the proposed method employs the mutual coherence and $\mathrm{AF}_{\mathrm{RMSE}}$ of the sensing matrix in SAIR as the design metric to guarantee the sensing matrix with good recovery capability.

3.2. Experiment for Imaging a Paper Cup with Hot Water

To further validate the efficiency of the proposed method, an experiment is carried out to image a paper cup with hot water. Fig. 8 shows the schematic of the experimental scenario. A paper cup with hot water is placed about 7 meters away from the prototype system. The temperature of the hot water is measured about 75°C, and the temperature of the room is measured about 23°C. The operating frequency of the prototype system is at W band. The antenna array configuration of the prototype system is an irregular array with 12 horn antennas, which is denoted by '○' symbols in Fig. 9. The beamwidth of each antenna is about 6 degrees. The bandwidth of the receive channel is 1 GHz. The visibility data are obtained from 12 channels of received signals after 2.4 GHz synchronous sampling and cross-correlation processing. Based on the obtained visibility data, different methods are used to realize the reconstruction of the observation scene.

Figures 9(a) and 9(b) give the receiving arrays used by the methods in [19] and [11], respectively. Fig. 9(c) shows the receiving array by the proposed method. The positions of the antenna elements by three methods are denoted by the symbols '$*$'.

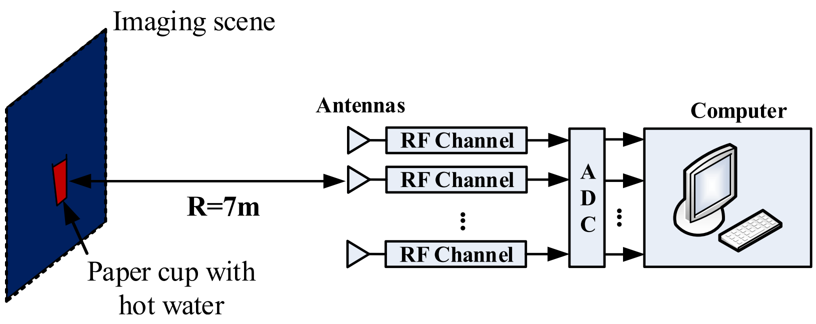

Figure 8. Schematic of the experimental measurement scenario.

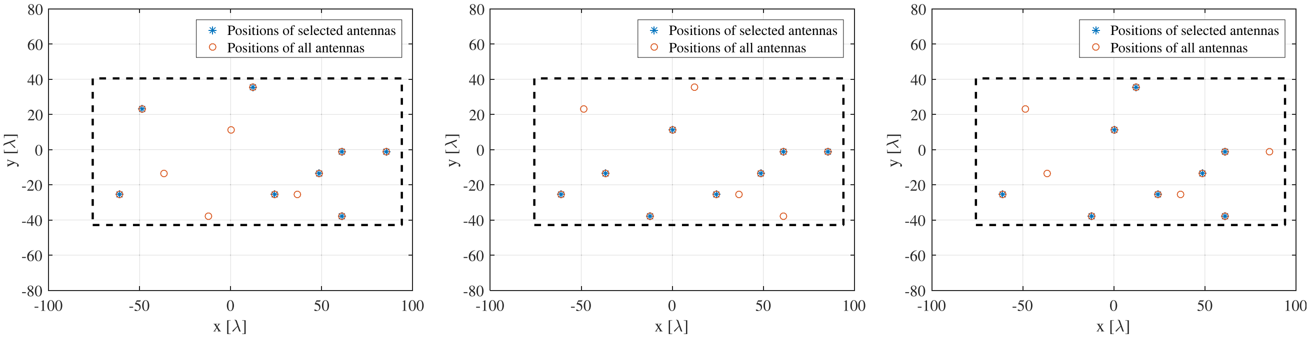

(a) (b) (c)

Figure 9. (a) Receiving array used by the method in [19]; (b) Receiving array used by the method in [11]; (c) Receiving array used by the proposed method in this paper.

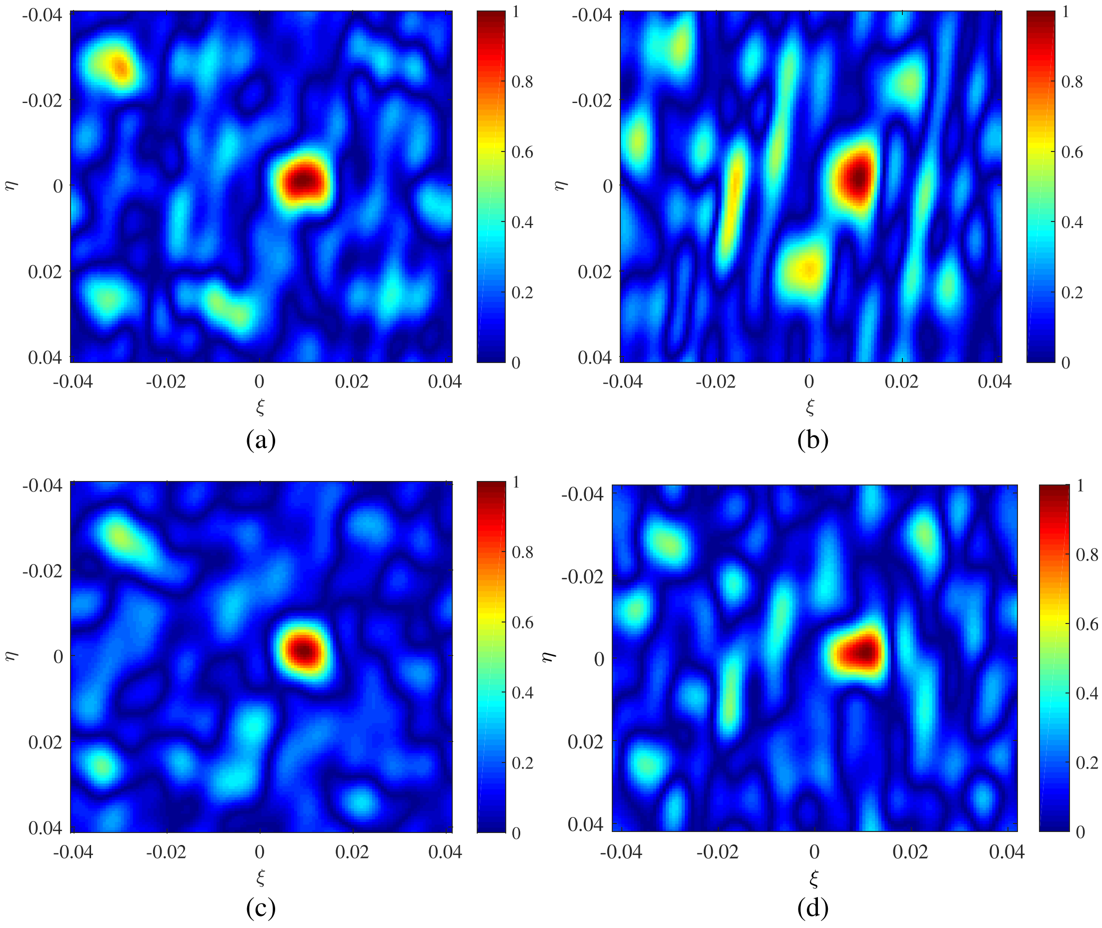

(a)

(b)

(c)

(d)

Figure 10. (a) Image recovered by the method in [19] with 8 receivers; (b) Image reconstructed by the method in [11] with 8 receivers; (c) Image reconstructed by the proposed method with 8 receivers; (d) Image reconstructed by the IDFT method with 12 receivers.

Figures 10(a) and 10(b) present the results reconstructed by using the methods in [19] and [11] with 8 elements, respectively. The size of the image reconstructed by each method is 128 × 128 pixels. Since the compressed measurement matrix is non-optimal, the performance of existing methods is under optimum, and the paper cup is difficult to distinguish from the image. Fig. 10(c) shows the image recovered by using the proposed method with 8 elements. The paper cup with hot water is well reconstructed with low ripples. The width of the paper cup in Fig. 10(c) is about 7 cm, which agrees well with the actual one. As reference, Fig. 10(d) shows the image recovered by using the IDFT method with 12 elements. Comparing Fig. 10(c) with Fig. 10(d), the proposed method with 8 receivers has similar imaging performance to the IDFT method with 12 receivers.

From Fig. 10, the proposed method has better recovery capability than the existing methods under the condition of the same number of receivers.

Through the simulations and experiments in this section, the feasibility of the proposed method is demonstrated. It can recover the BT image with better quality than the existing CS sparse reconstruction methods with the same number of receivers. The computation time and the resources consumed by different methods for reconstruction are listed in the following Table 3. The CPU of the computer is intel core i9 9900KF, and the RAM of the computer is 32 G.

For the same observation scene, the proposed method costs more calculation time than that of other methods. For different observation scenes, the calculation times of the same method are different due to the different numbers of pixels in different scenes. For all the observation scenes, the CPU and RAM resources occupied by different methods are similar.

Table 3. The computation time and the resources consumed by different methods.

	Computation time			Resource utilization	
	Earth	Ground	Paper Cup	CPU	RAM
Method in [11]	4.21 s	4.11 s	2.68 s	51%	21%
Method in [19]	4.18 s	5.95 s	2.41 s	49%	17%
Proposed method	4.43 s	6.03 s	2.96 s	51%	18%

4. CONCLUSIONS

The main contribution of this paper is to propose a new optimal sparse reconstruction method for imaging the BT map in SAIR. The proposed method employs both the mutual coherence and the $\mathrm{AF}_{\mathrm{RMSE}}$ of the compressed measurement matrix as the design metric to obtain the optimal receiving array to recover the BT image with a few receivers. Numerical and experimental results demonstrate that the proposed method has better recovery capabilities than the existing methods in SAIR. The method proposed in this paper provides an effective guide for reducing the complexity of the SAIR system in practical application.

ACKNOWLEDGMENT

This work was supported by the Science and Technology on Electronic Information Control Laboratory.

REFERENCES

1. Camps, A., J. Bará, I. C. Sanahuja, and F. Torres, "The processing of hexagonally sampled signals with standard rectangular techniques: Application to 2-D large aperture synthesis interferometric radiometers," *IEEE Trans. Geoscience and Remote Sensing*, Vol. 35, No. 1, 183–190, 1997.
2. McMullan, K. D., M. A. Brown, M. Martin-Neira, W. Rits, S. Ekholm, J. Matri, and J. Lemanczyk, "SMOS: The payload," *IEEE Trans. Geoscience and Remote Sensing*, Vol. 46, No. 3, 594–605, 2008.
3. Gaier, T., P. Kangaslahti, B. Lambrigtsen, I. Ramos-Perez, A. Tanner, D. McKague, C. Ruf, M. Flynn, Z. Zhang, R. Backhus, and D. Austerberry, "A 180 GHz prototype for a geostationary microwave imager/sounder-GeoSTAR-III," *2016 IEEE International Geoscience and Remote Sensing Symposium*, 2021–2023, 2016.
4. Kpré, E. L. and C. Decroze, "Passive coding technique applied to synthetic aperture interferometric radiometer," *IEEE Geoscience and Remote Sensing Letters*, Vol. 14, No. 8, 1193–1197, 2017.
5. Kpré, E. L. and C. Decroze, "Synthetic aperture interferometric imaging using a passive microwave coding device," *2016 IEEE Conference on Antenna Measurements Applications (CAMA)*, Oct. 23–27, 2016.
6. Kpré, E. L. and C. Decroze, "Passively coded synthetic aperture interferometric radiometer (CSAIR): Theory and measurement results," *European Conference on Antennas and Propagation*, Mar. 23–27, 2017.
7. Wikner, D. A., A. R. Luukanen, V. Chauhan, K. Greene, and B. Floyd, "Code-modulated interferometric imaging system using phased arrays," *Proc. SPIE*, Vol. 9830, 98300D.1–98300D.8, 2016.
8. Zhang, C., H. Liu, L. Niu, and J. Wu, "System design and preliminary tests of an L-band clock scan microwave interferometric radiometer," *2017 International Geoscience and Remote Sensing Symposium*, 715–718, 2017.

9. Zhang, C., H. Liu, L. Niu, and J. Wu, "CSMIR: An L-band clock scan microwave interferometric radiometer," *IEEE Journal of Selected Topics in Applied Earth Observations and Remote Sensing*, 1–9, 2018.
10. Li, S., X. Zhou, B. Ren, H.-J. Sun, and X. Lv, "A compressive sensing approach for synthetic aperture imaging radiometers," *Progress In Electromagnetics Research*, Vol. 135, 583–599, 2013.
11. Wang, J., Z. Gao, J. Gu, S. Li, X. Zhang, Z. Dong, Z. Zhao, F. Jiang, B. Qi, and P. Xian, "A new passive imaging technique based on compressed sensing for synthetic aperture interferometric radiometer," *IEEE Geoscience and Remote Sensing Letters*, Vol. 17, No. 11, 1938–1942, 2020.
12. Zhang, Y., "A robust reweighted L1-minimization imaging algorithm for passive millimeter wave SAIR in near field," *Sensors*, Vol. 15, No. 10, 24945–24960, 2015.
13. Chen, J., Y. Li, J. Wang, and Y. Li, "A compressive sensing imaging algorithm for millimeter-wave synthetic aperture imaging radiometer in near-field," *2013 Asia-Pacific Microwave Conference Proceedings*, 972–974, 2013.
14. Corbella, I., N. Duffo, M. Vall-llossera, et al., "The visibility function in interferometric aperture synthesis radiometry," *IEEE Trans. Geoscience and Remote Sensing*, Vol. 42, No. 8, 1677–1682, Aug. 2004.
15. Figueiredo, A. T., R. D. Nowak, and S. J. Wright, "Gradient projection for sparse reconstruction: Application to compressed sensing and other inverse problems," *IEEE Journal of Selected Topics in Signal Processing*, Vol. 1, No. 4, 586–597, 2007.
16. Candès, E. J. and M. Wakin, "An introduction to compressive sampling," *IEEE Signal Processing Magazine*, Vol. 25, No. 2, 21–30, Mar. 2008.
17. Romberg, J., "Imaging via compressive sampling," *IEEE Signal Processing Magazine*, Vol. 25, No. 2, 14–20, 2008.
18. Tropp, J. and A. Gilbert, "Signal recovery from random measurements via orthogonal matching pursuit," *IEEE Trans. Information Theory*, Vol. 53, No. 12, 4655–4666, Dec. 2007.
19. Obermeier, R. and J. A. Martinez-Lorenzo, "Sensing matrix design via mutual coherence minimization for electromagnetic compressive imaging applications," *IEEE Trans. on Computational Imaging*, Vol. 3, No. 2, 217–229, 2017.
20. Wu, J., C. Zhang, H. Liu, and J. Yan, "Performance analysis of circular antenna array for microwave interferometric radiometers," *IEEE Trans. Geoscience and Remote Sensing*, Vol. 55, No. 6, 3261–3271, 2017.